

## Full Length Article

# Microstructure and mechanical behavior of an additive manufactured (AM) WE43-Mg alloy



Sindhura Gangireddy<sup>a,\*</sup>, Bharat Gwalani<sup>a,b</sup>, Kaimiao Liu<sup>b</sup>, Eric J. Faierson<sup>c</sup>, Rajiv S. Mishra<sup>a,b</sup>

<sup>a</sup> Advanced Materials and Manufacturing Processes Institute, University of North Texas, Denton, TX, USA

<sup>b</sup> Materials Science and Engineering, University of North Texas, Denton, TX, USA

<sup>c</sup> Quad City Manufacturing Lab – Western Illinois University, Rock Island, IL, USA

## ARTICLE INFO

**Keywords:**  
WE-43 Mg alloy  
Powder bed fusion  
Dynamic mechanical response  
Porosity  
Electron microscopy

## ABSTRACT

Magnesium alloys are highly attractive in aerospace and auto industries due to their high strength-to-weight ratio. Additive manufacturing of Mg alloys can further save cost from materials and machining time. This paper investigates the microstructure and dynamic mechanical behavior of WE-43 Mg alloy built through the powder bed fusion process. Samples from four different combinations of processing parameters were built. These builds were studied in both as-built and hot isostatically pressed conditions. The resultant complex microstructures were studied under scanning and transmission electron microscopes while their dynamic mechanical behavior was evaluated using a split-Hopkinson pressure bar testing system. Effects of initial porosity and microstructural evolution during HIP treatment on mechanical response are discussed.

## 1. Introduction

Magnesium alloys exhibit high specific strength and are highly attractive as low weight structural materials in aerospace, automotive, biomedical, and other industries where weight reduction is essential [1–5]. Mg alloys with rare earth alloying elements are certified as non-flammable [6,7]. WE-43 Mg with 4 wt% Y, 3.3 wt% Nd (Rare earth element RE), and 0.5 wt% Zr has recently garnered interest due to its high creep resistance, retention of high temperature strength, and corrosion resistance [8,9]. This composition can support a combination both solid solution and precipitation hardening mechanisms [10,11]. Age hardening treatments determine the precipitation sequence of intermetallic phase formation and distribution in this alloy [12,13] and the mechanical properties are highly influenced by the characteristic Mg-Nd-Y precipitate phases [14–16].

Additive manufacturing (AM) is a rapidly growing technology of building components in layers. In powder bed fusion (PBF) process, metal powder is spread across an area using a recoating mechanism and then selectively melted using a heat source such as a laser. PBF is highly desired for a variety of complex geometries, such as internal channels, which cannot be fabricated using conventional subtractive machining technology. Over the years, SLM has become quite well established for titanium, steel and iron, cobalt, nickel, and aluminium alloys [17–21]. As additive manufacturing of Mg alloys has also caught interest, there have been numerous efforts in the recent years on achieving successful

laser melting, overcoming the difficulties involved due to their low vaporizing temperatures and reactive nature, and creating process windows for formability of pure Mg, and Mg-Al, Mg-Mn and AZ91 alloys [22–28].

As WE-43 Mg is a high strength alloy with good ambient and high temperature mechanical properties with good corrosion resistance, some research groups have extensively studied the WE-43 Mg cast microstructure and its evolution with different types of heat treatments designed for precipitation hardening [29,30]. More recently, there have also been investigations into the quasi-static and dynamic behavior of WE-43 Mg cast and T5-heat treated sheet alloys [31–34]. However, the literature on additively manufactured WE-43 Mg has been extremely limited, with just two conference proceedings by Jauer et al. [35] and Tandon et al. [36] with very brief microstructural analysis and single quasi-static tensile data points. To the best of our knowledge, there have not been any other investigations on additively built and heat treated WE-43 Mg combining microstructural characterization and mechanical evaluation.

Successful fabrication of WE-43 Mg alloy components from additive manufacturing still requires a thorough understanding of the equilibrium and meta-stable intermetallic phases that form from the rapid heating and cooling cycles involved in laser melting, and how they affect the mechanical performance. In this study, we examined the microstructures and dynamic mechanical responses of WE-43 Mg additively built from four different SLM processing conditions and in two

\* Corresponding author.

E-mail address: [Sindhu.g.reddy@gmail.com](mailto:Sindhu.g.reddy@gmail.com) (S. Gangireddy).

conditions, as-built and hot isostatically pressed (HIP'ed). Cylindrical specimens were built for dynamic deformation testing using split-Hopkinson pressure bar (SHPB). Scanning and transmission electron microscopes were used to characterize the initial microstructures in the as-built and heat treated conditions. Correlation of dynamic flow stresses and their fracture strains to the microstructural observations is reported.

## 2. Experimental Procedure

### 2.1. Material preparation

Cylindrical SHPB specimens of WE-43 Mg with dimensions of 5 mm diameter and 5 mm height were built on an EOS M270 PBF system. Powder of WE-43, under commercial name MAP + 43, was sourced from vendor Magnesium Elektron. The powder had a particle size ranging from 15 to 63  $\mu\text{m}$ . The build was conducted in argon gas with an O<sub>2</sub> concentration less than 0.1% and the build platform temperature was 35 °C. Four combinations of varying laser build parameters were utilized, which included: laser power between 135–195 W, scan speed between 800–1200 mm/s, and hatch spacing between 0.20–0.25 mm. The laser spot size and layer thickness were 100  $\mu\text{m}$  and 0.03 mm, respectively, and maintained constant across all builds. Laser scan pattern was rotated 67° each layer. All the samples were built vertically, with the cylinders' axes aligned parallel to the growth direction. One set of the four builds were tested in as-built condition and a second set was subjected to hot isostatic pressing (HIP) at 350 °C, 15000 psi for 2 h, after which they were tested. Subjecting the builds to both high temperature and isostatic gas pressure is anticipated to lead to reduction of porosity and modification of microstructure to improve mechanical properties by precipitation hardening.

### 2.2. Microstructural characterization

Samples were sectioned at their center along an XZ plane for both as-built and HIP conditions. A 2500  $\mu\text{m}$  x 2500  $\mu\text{m}$  area, representing a significant portion of the total sample size, was analyzed using ImageJ software to calculate porosity. In addition, water immersion (Archimedes/densimeter) was used to measure the density and then porosity estimates were made from comparison with density measurement of the cast material. Detailed microstructures of the nearly fully dense Sample#1 as well as Sample#9 with largest porosity were investigated. As-built and HIP conditions of both samples were studied using FEI NanoSEM 230 for back scattered electron microscopy (BSE-SEM) as well as electron dispersive x-ray spectroscopy (EDAX) at low magnification (3000 X) to high magnification (25,000 X). Further higher magnification studies were performed using Phillips EM420 FEI transmission electron microscope (TEM) and energy dispersive analysis using Technai G2 F20 high resolution analytical transmission microscope (STEM-EDS). High resolution Rigaku Ultima III X-Ray Diffractometer (XRD) was used for X-Ray diffraction pattern analysis.

### 2.3. SHPB testing

Dynamic compression tests were conducted on these cylindrical specimens at a strain rate of 1000  $\text{s}^{-1}$  on the 8 different conditions using a split-Hopkinson pressure bar (SHPB). The commercial SHPB unit procured from REL Inc. is depicted in Fig. 1 along with a schematic illustration of the major components. In compression mode of SHPB, the sample is placed between two long bars of 10 m length and 18 mm diameter made of maraging steel with yield strength of > 2 GPa. The first bar on the left is the incident bar and the second bar on the right is termed transmission bar. The incident bar is impacted by a fast moving projectile powered from a pressurized air gun. This striker bar is also of maraging steel and has similar diameter as the incident and transmission bars, and therefore has a similar acoustic impedance. The length of

the striker bar, which determines the duration of the loading pulse, was 30 cm. The impact of striker bar on the incident bar creates an elastic wave at the interface which travels through the incident bar, and upon reaching the specimen, the acoustic impedance difference results in only part of the wave going through the specimen into the transmission bar while the rest is reflected back. The amplitude and duration of these elastic wave pulses are recorded using two strain gauges placed at 5 m distance from the specimen on either bar. This separation allows for clear recording of the incident and reflected wave pulses in the first strain gauge without time overlap. A self-triggered oscilloscope recorded the strain gauge data at a high rate of 1 M/s. The strain gauge signals are amplified for accuracy. Then the incident, reflected and transmitted waves were analyzed according to one dimensional elastic wave theory to obtain the stress, strain rate and strain [37].

$$\sigma(t) = \frac{A_B E \varepsilon_t(t)}{A_S}$$

$$\dot{\varepsilon}(t) = \frac{2 c_o \varepsilon_r(t)}{l_S}$$

$$\varepsilon(t) = \int_{t_i}^{t_f} \dot{\varepsilon}(t) dt$$

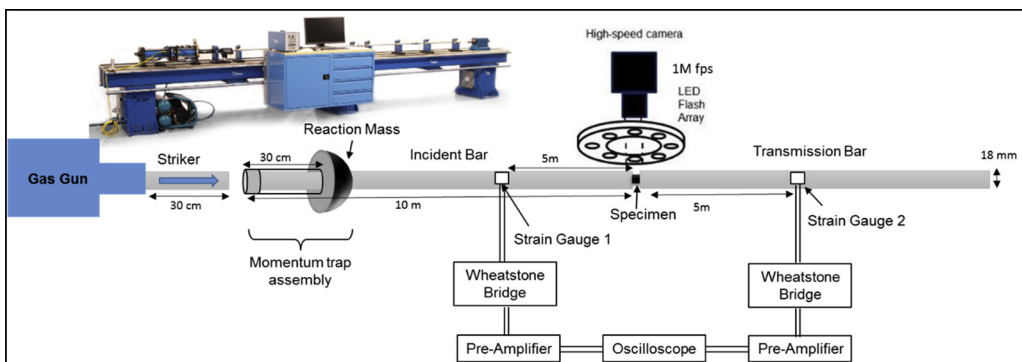
where  $A_B A_S$  is the cross-sectional area of the Bar,  $A_S$   $A_S$  and  $l_S$   $l_S$  are the sample cross-sectional area and length respectively,  $E$  and  $c_o$  are the elastic modulus and elastic wave speed of the Bar,  $\varepsilon_t$ ,  $\varepsilon_t$  and  $\varepsilon_r$ ,  $\varepsilon_r$  are the transmitted and reflected wave strains. The SHPB system was also equipped with a momentum trap assembly which enables single loading of the specimen by moving the incident bar away from the sample to prevent multiple loadings of the reflected waves. The measurement accuracy of flow stresses from this method and the associated error analysis have been discussed in detail in a previous publication [38].

## 3. Results

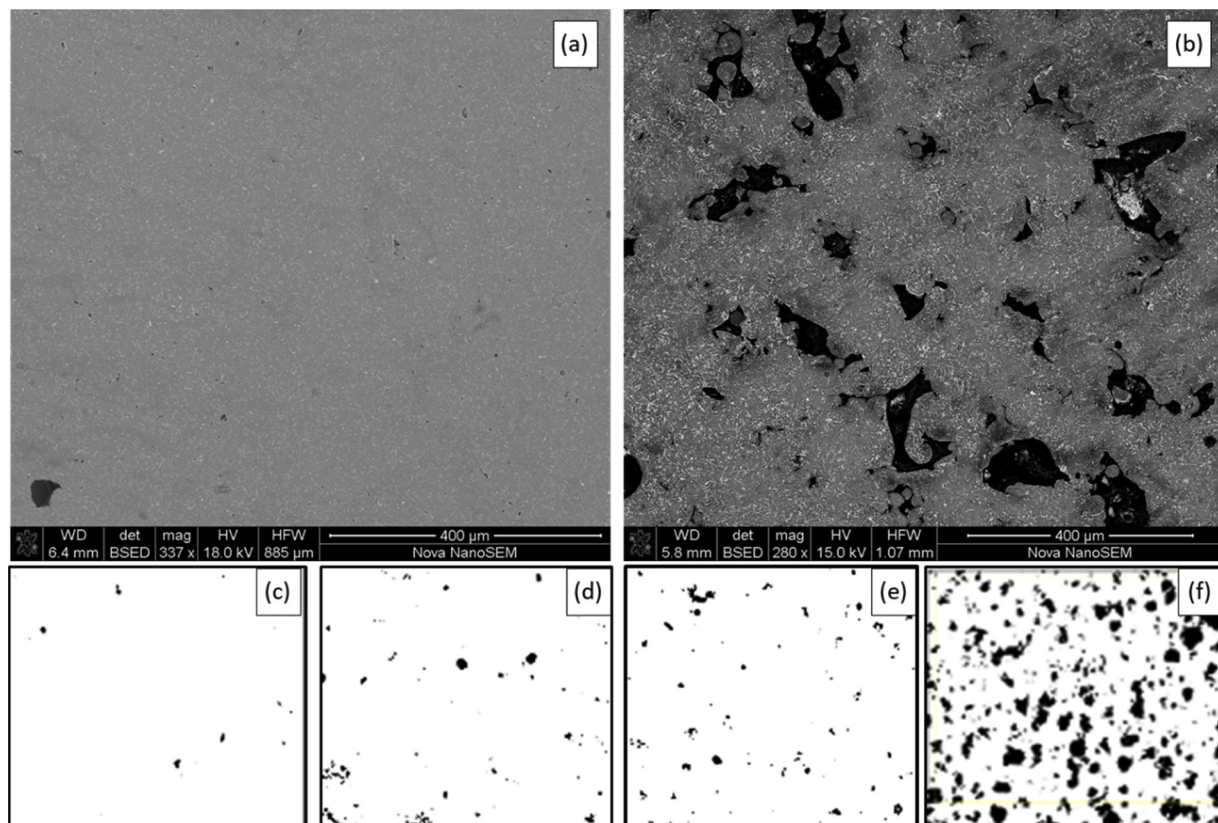
### 3.1. Porosity in samples

Fig. 2(a) and (b) highlight the difference in porosity of the as-built builds with different processing parameters. These SEM images contrast a nearly full dense Sample#1 with an obviously porous Sample#9. Optical micrographs of polished XZ surfaces of 2500  $\mu\text{m}$  x 2500  $\mu\text{m}$  area are obtained in each of the four as-built specimens. These micrographs were analyzed in ImageJ software to obtain thresholded images as shown in Fig. 2(c-f), from which porosities were estimated. A second assessment of porosity was obtained from densimeter measurements from Archimedes principle and comparison to the density of fully dense cast material. Table 1 summarizes the four sets of build parameters, the porosity estimates from image analysis via metallography and those from density measurements. Table 1 also summarizes the relative change in porosity after HIP treatment.

It can be seen that porosities varied widely across the four builds. Image analysis revealed Sample#1 to be nearly fully dense with 0.4% whereas its density 1.84gm/cc compared to 1.845gm/cc of cast sample indicated a porosity of 0.27%. On the other extreme, Sample#9 showed a high level of porosity of 17% from image analysis and 12.41% porosity from density estimation. In most specimens, the estimates of porosity from image analysis and density measurements matched closely as seen in Table 1, except in Sample#9. In this case, the estimate from density measurement is deemed more reliable. Recovery of the initial porosity in as-built material was attempted through a high temperature HIP treatment. The extent of recovery was much greater at higher porosity levels, e.g. in Sample#9 porosity was reduced from 12.4% to 2.7% after HIP. At very small porosity levels such as seen in Sample#1, densification from HIP was quite limited. The temperature of HIP treatment, 350 °C, is ~ 0.6 T<sub>m</sub> of the alloy [39] and sufficient to enable diffusion controlled neck growth to reduce large porosity [40].



**Fig. 1.** Schematic illustration of the compression mode split-Hopkinson pressure bar used for dynamic deformation of the specimens at  $1000 \text{ s}^{-1}$  strain rate. A real picture of the apparatus is also embedded.



**Fig. 2.** SEM images and thresholded optical images of WE43-Mg specimens showing varying amounts of porosity: (a–b) SEM images demonstrating the contrast in porosity of (a) Sample# 1, and (b) Sample# 9. (c–f) Thresholded optical images of the four conditions used in estimation of porosity from processing parameter variation: (c) Sample#1 (195 W, 800 mm/s, 0.2 mm) showing 0.4% porosity, (d) Sample# 4 (195 W, 800 mm/s, 0.25 mm) with 1% porosity (e) Sample# 7 (195 W, 1200 mm/s, 0.2 mm) with 2.5% porosity (d) Sample# 9 (135 W, 1200 mm/s, 0.2 mm) with 17% porosity.

**Table 1**

Build parameters in the 4 samples produced by variation of laser power, scan speed, and hatch-spacing. The porosities in the as-built and after HIP conditions are compared.

Sample #	Laser Power (W)	Scan Speed (mm/s)	Hatch Spacing (mm)	As-Built Porosity from image analysis (%)	As-Built Density (gm/cc)	As-Built Porosity from Density Measurement (%)	HIP Porosity (%)
1	195	800	0.20	0.4	1.84	0.3	0.3
4	195	800	0.25	1	1.813	1.7	0.6
7	195	1200	0.20	2.5	1.783	3.4	0.7
9	135	1200	0.20	17	1.616	12.4	2.7
<b>Fully dense cast condition</b>					1.845	0	

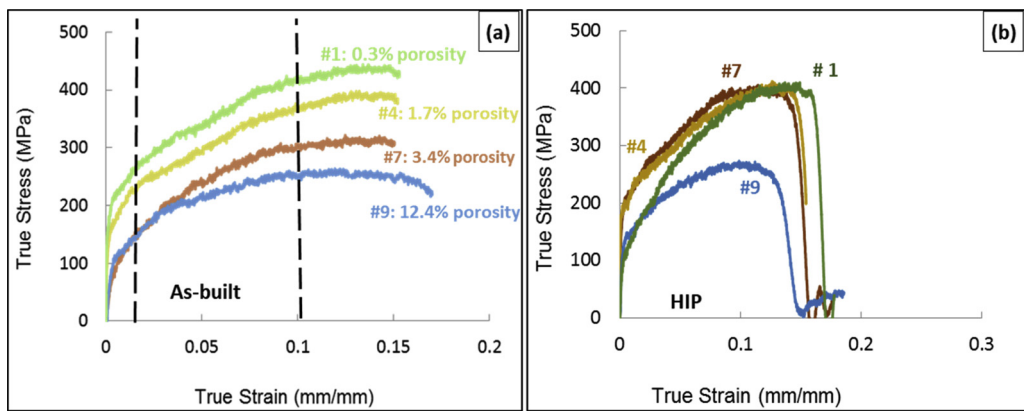


**Fig. 3.** (a) Dynamic stress-strain curves from SHPB testing at  $1000\text{ s}^{-1}$  on (a) as-built WE-43 Mg cylinders, (b) after HIP treatment.

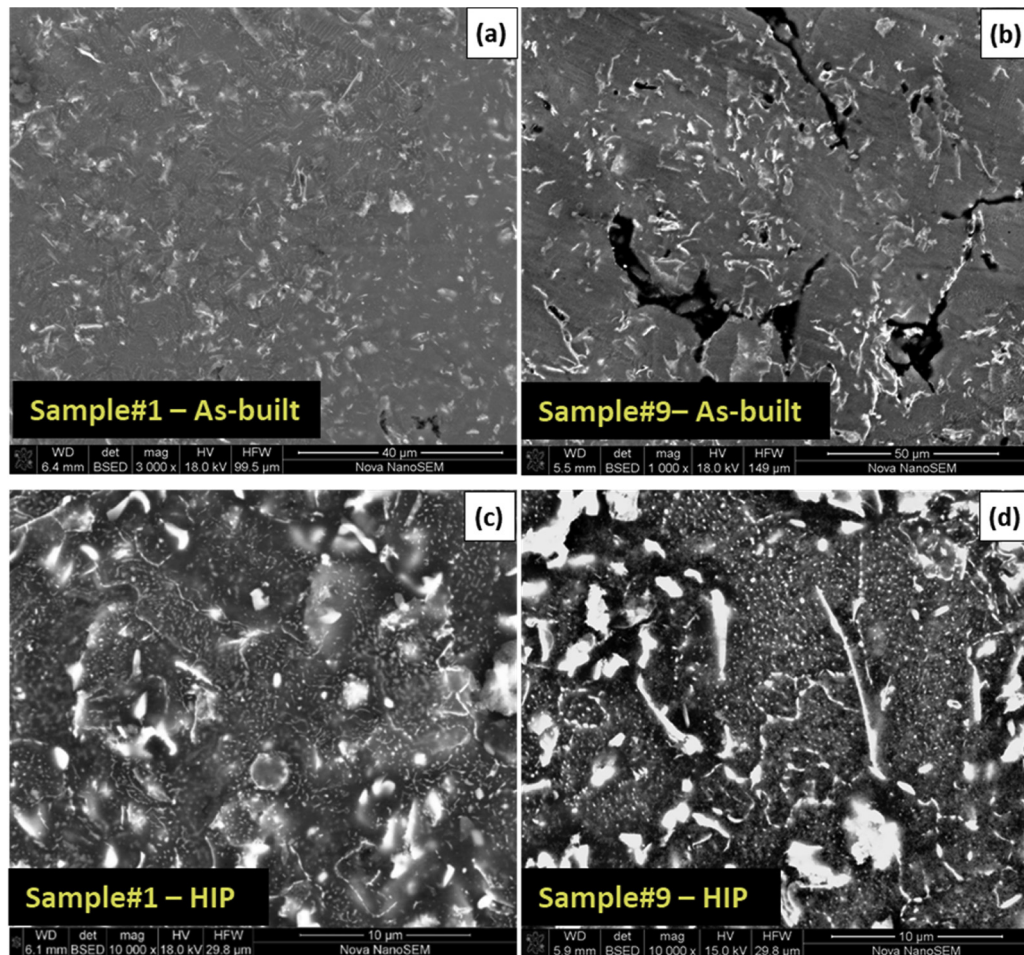


**Fig. 4.** Comparison of the microstructures of Sample#1 with 0.3% porosity and Sample#9 with 12.4% porosity illustrating homogeneity. Scanning electron microscopy images of (a) as-built Sample#1, (b) as-built Sample#9, (c) HIP'ed Sample#1, and (d) HIP'ed Sample#9.

But the time duration of 2 h appears to be inadequate for further grain boundary migration to eliminate the small spherodized pores that still remain trapped [40,41]. The relative improvement in porosity in the different samples can be observed from Table 1.

### 3.2. Mechanical properties

Dynamic true stress-strain curves from SHPB testing of the four builds in both as-built and HIP'ed conditions are depicted in Fig. 3. It can be seen from Fig. 3(a) that the flow stresses of the as-built material

dropped steadily with increasing porosity level in the builds. The nearly fully dense Sample#1 with 0.3% porosity shows an initial dynamic strength of  $\sim 240\text{ MPa}$  increasing to  $\sim 420\text{ MPa}$  by 0.1 strain. At highest porosity of 12.4%, Sample#9 had half this strength and demonstrated much lower  $\sigma \sim 117\text{ MPa}$  at 1% strain and 245 MPa at 10% strain. Fig. 3(b) shows the dynamic stress-strain curves of these four builds after HIP treatment. All the HIP treated samples failed by 45° shear around 15% strain, showing a drastic drop in strength.

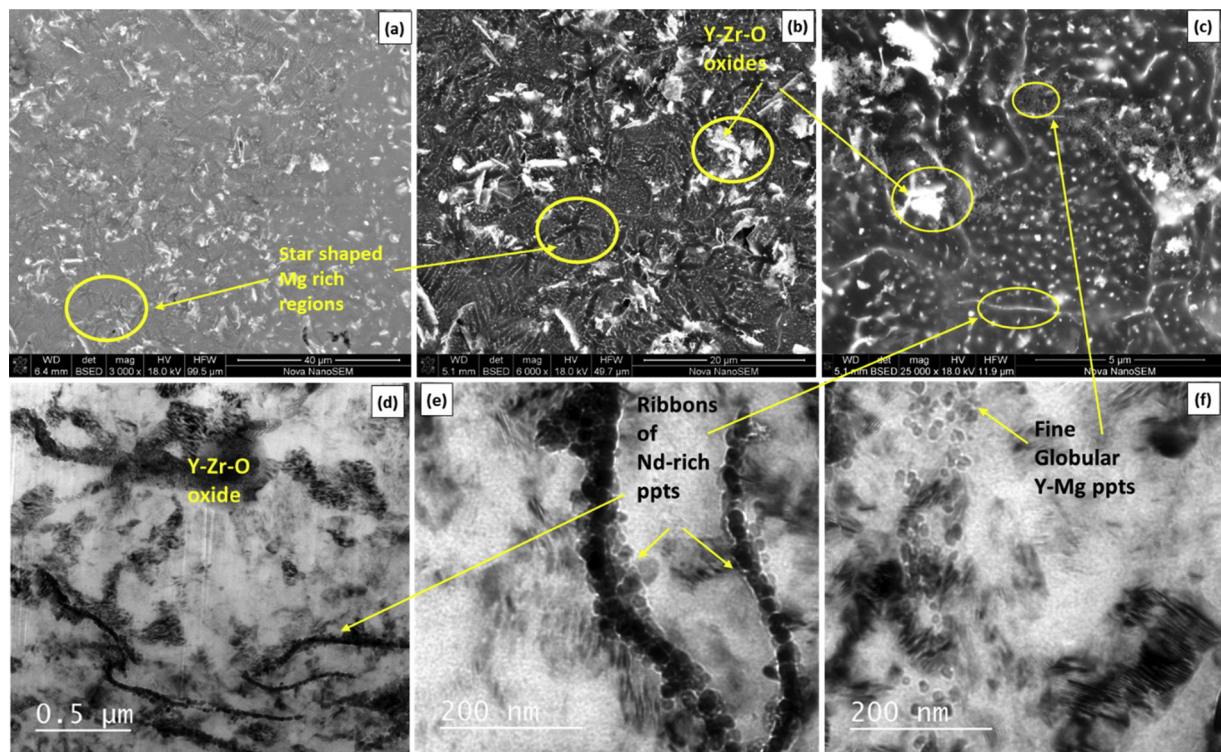


**Fig. 5.** Electron Microscopy images of as-built WE43-Mg Sample#1 (195 W, 800 mm/s, 0.2 mm) with 0.3% porosity: (a–c) BSE images of 3000 X, 6000 X, and 25,000 X magnification, (d–e) TEM images highlighting individual particle/ribbon features in higher magnification.

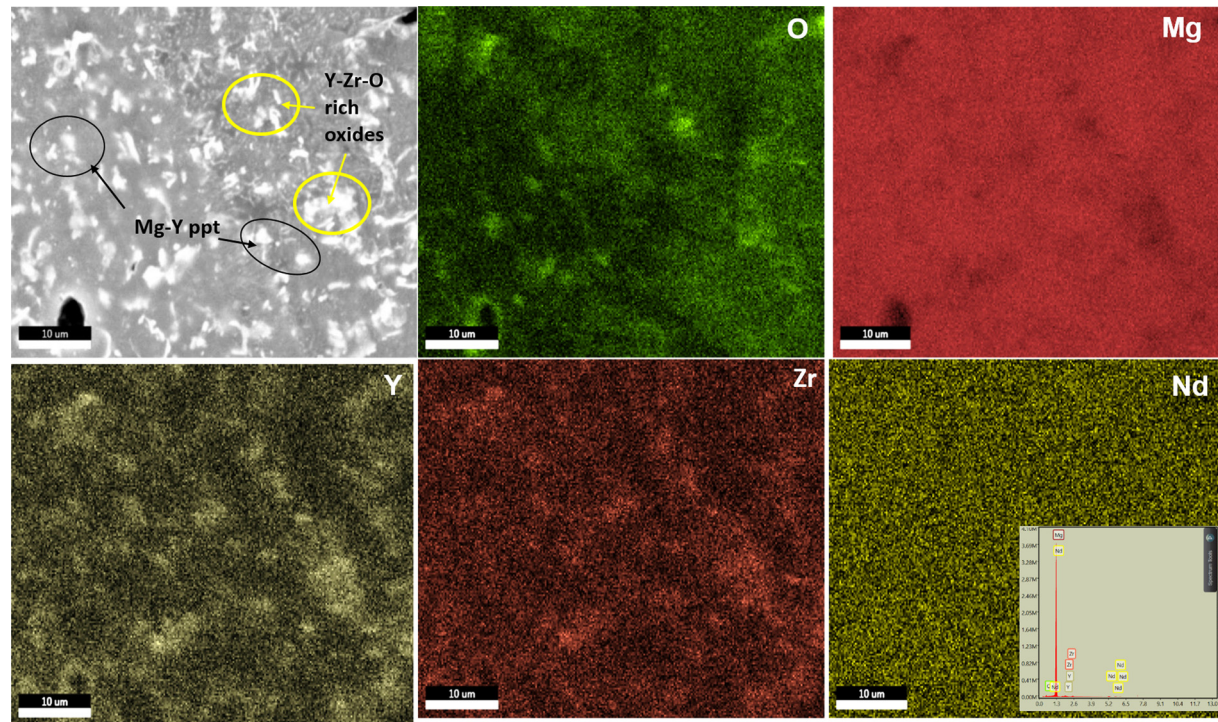


**Fig. 6.** SEM-EDAX elemental maps of as-built WE43-Mg Sample#1 (195 W, 800 mm/s, 0.2 mm, 0.3% porosity) highlighting Y-Zr-O rich regions which indicate oxides, and O-depleted Y-rich regions conjecturing Y-rich precipitates of Mg-Y. The EDS spectrum of the region is embedded in Nd-Map.

### 3.3. Microstructures

Microstructures of additive WE-43 Mg alloy can be quite complex due to its precipitation hardenable nature [29,30] which during the rapid heating and cooling cycles of SLM process can result in a variety

of precipitates [35]. Presence of oxides, especially  $\text{Y}_2\text{O}_3$  in Y powder with high affinity of oxygen, from initial powders or formation from reduction of  $\text{MgO}$  during melting, is also a possibility [36]. Hence a thorough microstructural investigation was necessary.

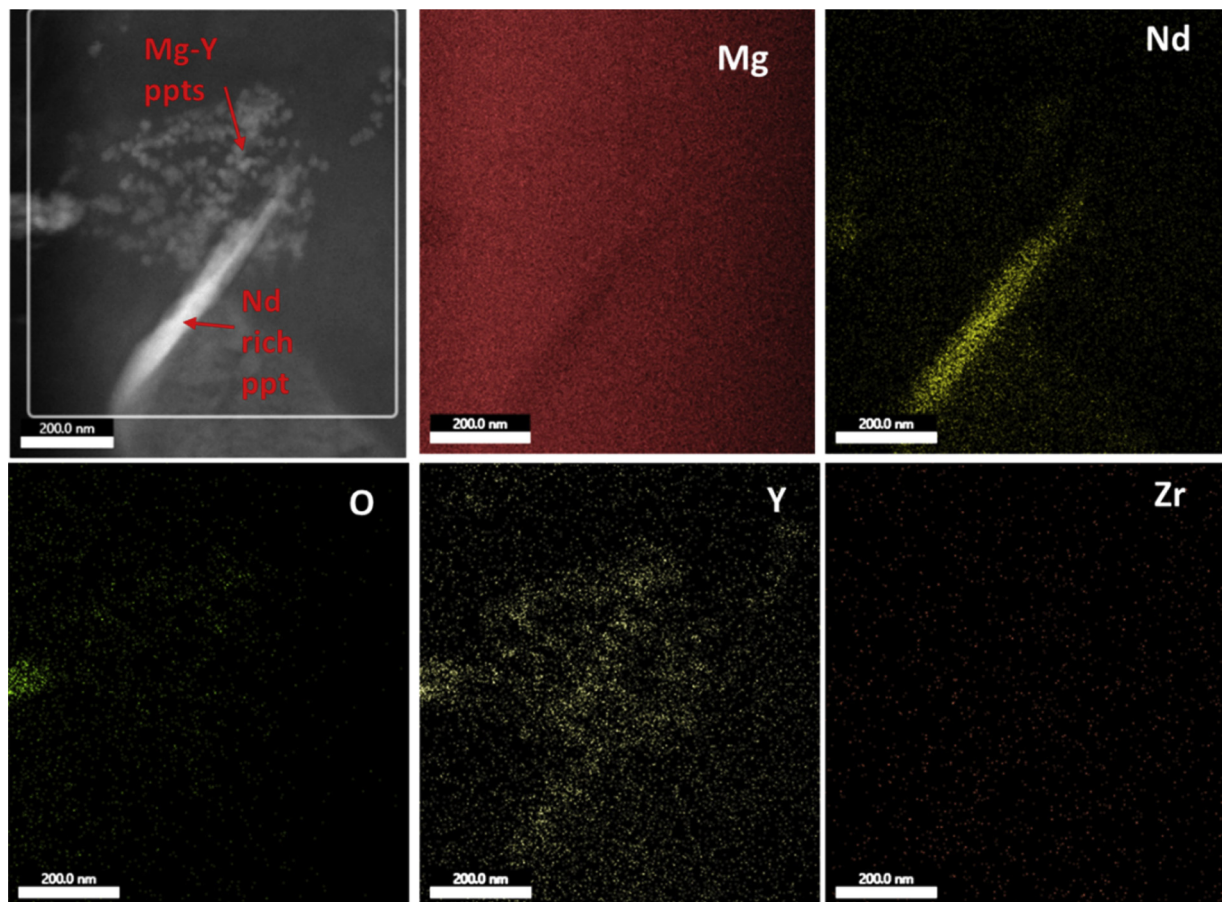


**Fig. 7.** STEM-EDS elemental maps of as-built WE43-Mg Sample#1 (195 W, 800 mm/s, 0.2 mm, 0.3% porosity) highlighting Nd-rich ribbon region and Y-rich minuscule globules.

### 3.3.1. Fully dense vs. porous builds

The microstructures in the four builds were identical despite the variation in processing parameters and thus resulting wide porosity ranges. Comparison of SEM images across the builds with drastically different porosities, nearly fully dense Sample#1 with 0.3% porosity and porous Sample#9 with 12.4% porosity, is presented in Fig. 4. Fig. 4(a-b) compare the microstructural features in as-built conditions of these two builds whereas Fig. 4(c-d) illustrate the similarity in their HIP conditions. This homogeneity in microstructures across these builds suggested that the porosity did not originate from melting/solidification issues. Further investigation is conducted through higher magnification SEM, SEM-EDS, TEM, TEM-EDS to understand the microstructural features in detail and presented in the sections below.

### 3.3.2. As-built condition

Descriptions in previous studies, which only reported formation of  $\text{Y}_2\text{O}_3$ , and Y-, Nd- rich precipitates [35,36], were severe understatement for the exceedingly complex microstructures we observed. BSE images of the nearly fully dense Sample#1 from 3000X to 25000X magnification in Fig. 5(a–c) showed several curious features. TEM images in Fig. 5(d–e) were acquired for high magnification imaging. SEM-EDAX was used to identify the segregation of elements in the coarser features, Fig. 6. Five pointed star-shaped regions are seen in dark contrast, which have not been reported previously elsewhere. The star shaped regions were typically Mg-rich and since Mg has lower atomic weight than the alloying elements, these 10  $\mu\text{m}$  wide features appear in dark contrast in BSE. A multitude of particles and ribbon like features of several different length scales appear in bright contrast. There is a large overlap of O-rich regions with Y- and Zr-rich regions, appearing in bright contrast

in the BSE image. Simultaneously these regions were also depleted in Mg, indicating these were Y-, Zr- oxide regions of  $\sim 2\text{--}5 \mu\text{m}$  diameter. The high magnification TEM image in Fig. 5(d) shows these oxide regions to be in fact composed to multiple smaller spherical particles indicating they formed from the initial powder material which was passivated for safe handling. There were additionally some Y-rich regions that were depleted in O, and hence must be Y-rich precipitates of 1–3  $\mu\text{m}$  diameter.  $\text{Mg}_{24}\text{Y}_5$  intermetallic precipitates of similar length scale  $\sim 1 \mu\text{m}$  have been reported in the cast microstructure by previous studies [29,31] and are predicted from the phase diagram as well [42]. Nd, on the other hand, did not show significant segregation at this magnification level. STEM-EDS at higher magnification level, shown in Fig. 7, captured the elemental composition of finer features. The ribbon features in Fig. 5(b–c) were revealed to be clusters of precipitates in the TEM (Fig. 5(d–e)), and to be Nd-rich from STEM-EDS (Fig. 7), i.e., Mg-Nd precipitates. The scale of  $\text{Mg}_{41}\text{Nd}_{5}$  intermetallic phases reported in the cast microstructures are significantly larger, Rzyynchon et al observed intragranular 3  $\mu\text{m}$  wide  $\text{Mg}_{41}\text{Nd}_{5}$  [29] while Xiang et al described a eutectic phase whose  $\beta$ -platelets were composed of  $\text{Mg}_{24}\text{Re}_5$  where Re = Y, Nd, Gd with 500nm width [31]. The Nd-rich ribbons observed in this additive material has a very high aspect ratio and very small width, only 20–30 nm. The minuscule globular particles of  $< 10 \text{ nm}$  diameter were mainly Y-rich, without O, signifying they were also Mg-Y precipitates.

### 3.3.3. HIP'ed condition

Scanning electron microscope images of Sample#1 after HIP at 4000X–20000X magnification are shown in Fig. 8(a–c), while high magnification TEM images are depicted in Fig. 8(d–e). SEM EDAX maps

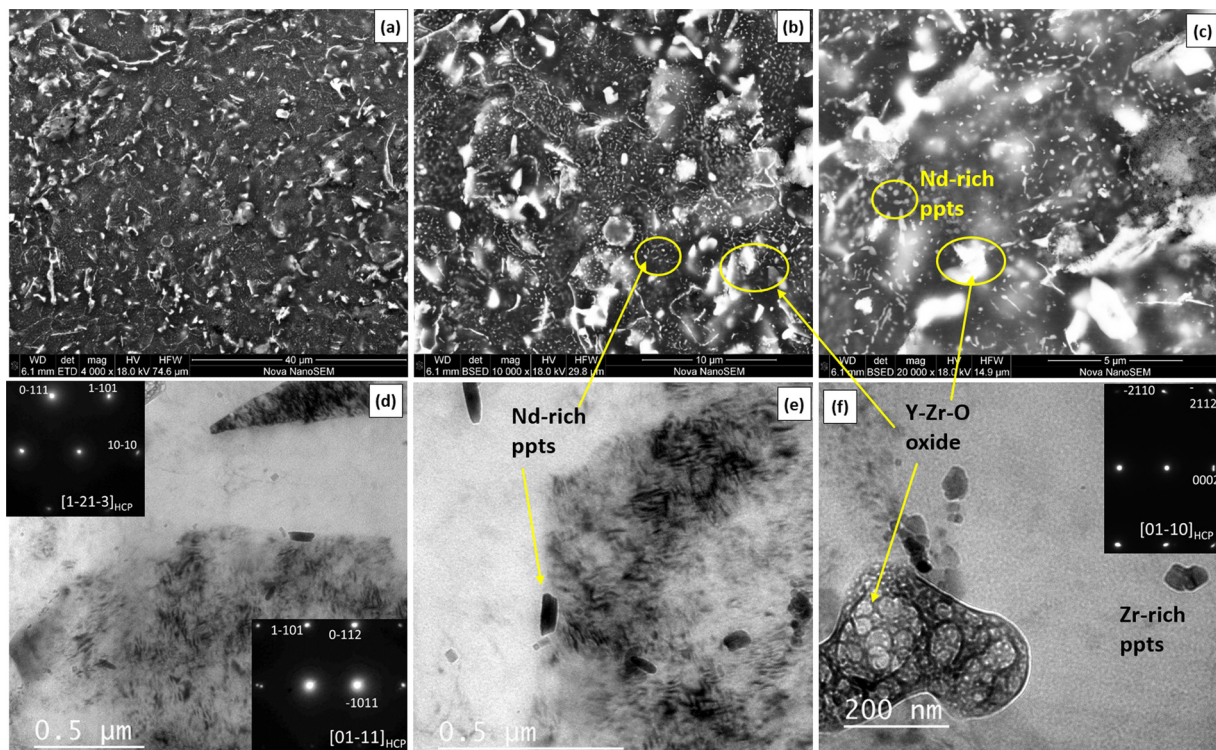


**Fig. 8.** Electron Microscopy images of HIP'ed WE43-Mg Sample#1 (195 W, 800 mm/s, 0.2 mm) with 0.4% porosity: (a–c) BSE images of 4000X, 10000X, and 20000X magnification, (d–e) TEM images highlighting the oxides and numerous plate-like Nd-rich precipitates at higher magnification. Insets show SADP patterns of the matrix in HCP crystal structure.

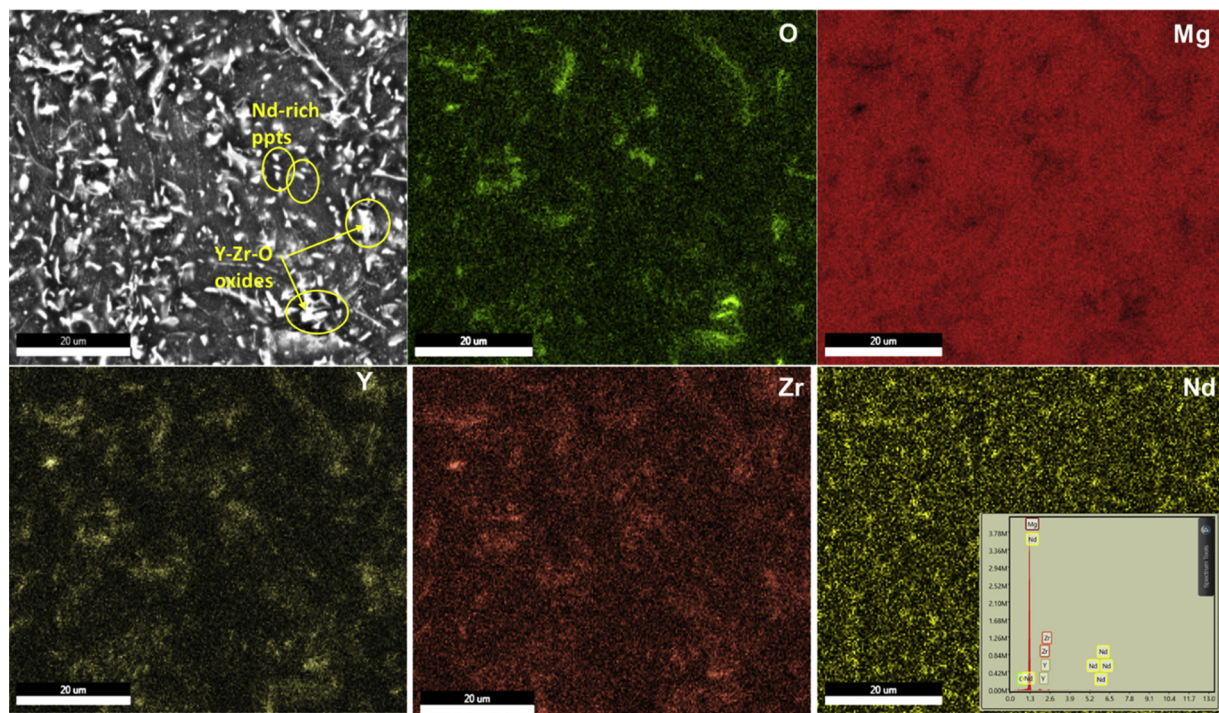


**Fig. 9.** SEM-EDAX elemental maps of HIP'ed WE43-Mg Sample#1 (195 W, 800 mm/s, 0.2 mm, 0.4% porosity) highlighting Y-Zr-O rich regions which indicate oxides, and plate-like Nd-rich precipitates. EDS spectrum of the region is embedded in Nd –map.

In Fig. 9 show the elemental segregation in coarse features while STEM-EDS mapping in Fig. 10 demonstrates elemental composition in the fine features. After HIP, the microstructures remain still complex but with several distinct changes. Firstly, the long ribbon features identified to be Nd-rich precipitates in as-built condition (Fig. 5(e)) disappeared.

These were replaced with numerous smaller precipitates. SEM-EDAX in Fig. 9 shows these regions to be Nd-rich. Similarly STEM-EDS in Fig. 10 also shows a 350 nm sized faceted Nd-rich precipitate. It appears that the Nd-rich ribbons in as-built material broke up and transformed into shorter but thicker plate-shaped precipitates after the HIP treatment.

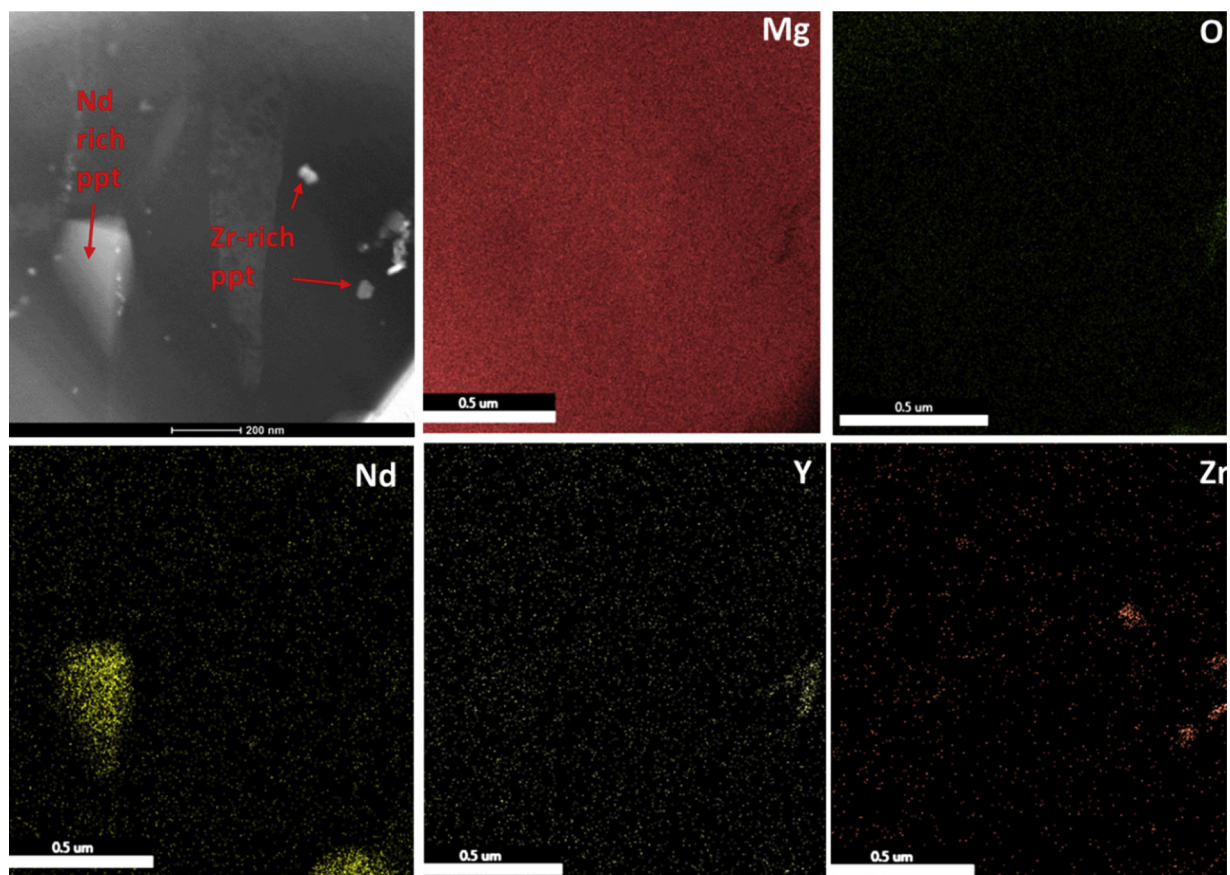


**Fig. 10.** STEM-EDS elemental maps of HIP'ed WE43-Mg Sample#1 (195 W, 800 mm/s, 0.2 mm, 0.4% porosity) highlighting large Nd-rich precipitate, smaller Zr-rich precipitate, Zr-Y-O rich oxides along with a large oxide rich in Mg.

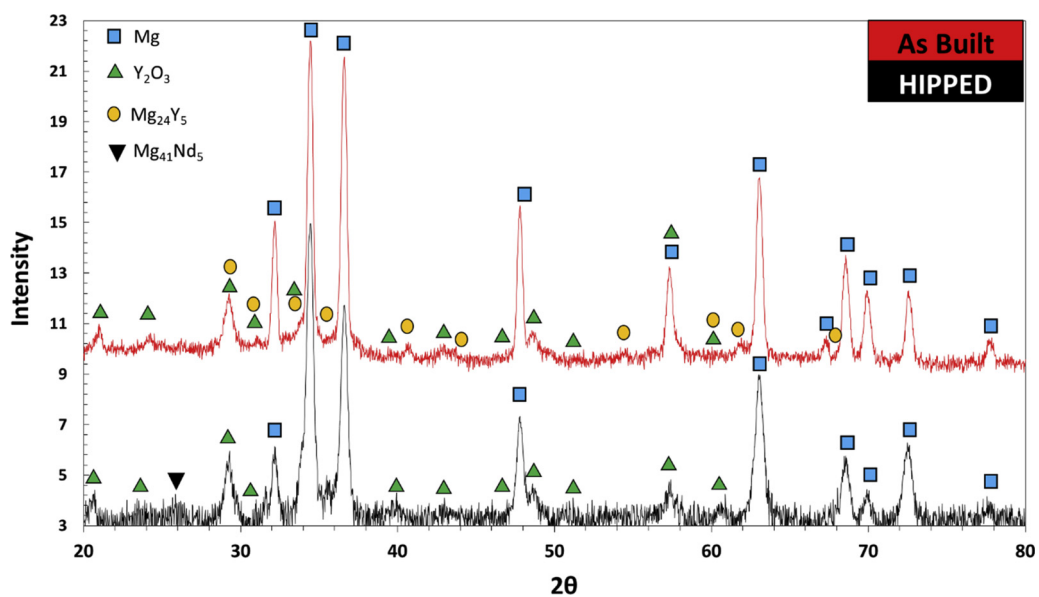


**Fig. 11.** Comparison of XRD diffraction peaks of as-built vs. HIP'ed WE-43 Mg cylinders.

The larger of these features were  $\sim 100\text{--}500\text{ nm}$  in diameter. These were detected in SEM-EDAX as well and the Nd-elemental distribution maps shows segregation. There are also large bright regions, Fig. 8(c), which SEM-EDAX shows to be Y-, Zr-, and O- rich, inferring these were oxides, similar to the ones observed in as-built condition. STEM EDS in Fig. 10 shows new features appearing after heat treatment: Zr-rich regions depleted in O and Y, and hence must Zr-Mg precipitates. Selected

area diffraction patterns (SADPs) in the insets of Fig. 8(d-e) show that the matrix phase is HCP crystal structure. The lack of any superlattice spots in these SADP patterns indicates that there are no coherent intermetallics in the material. So the only precipitates in these microstructures are those imaged by BF-TEM.

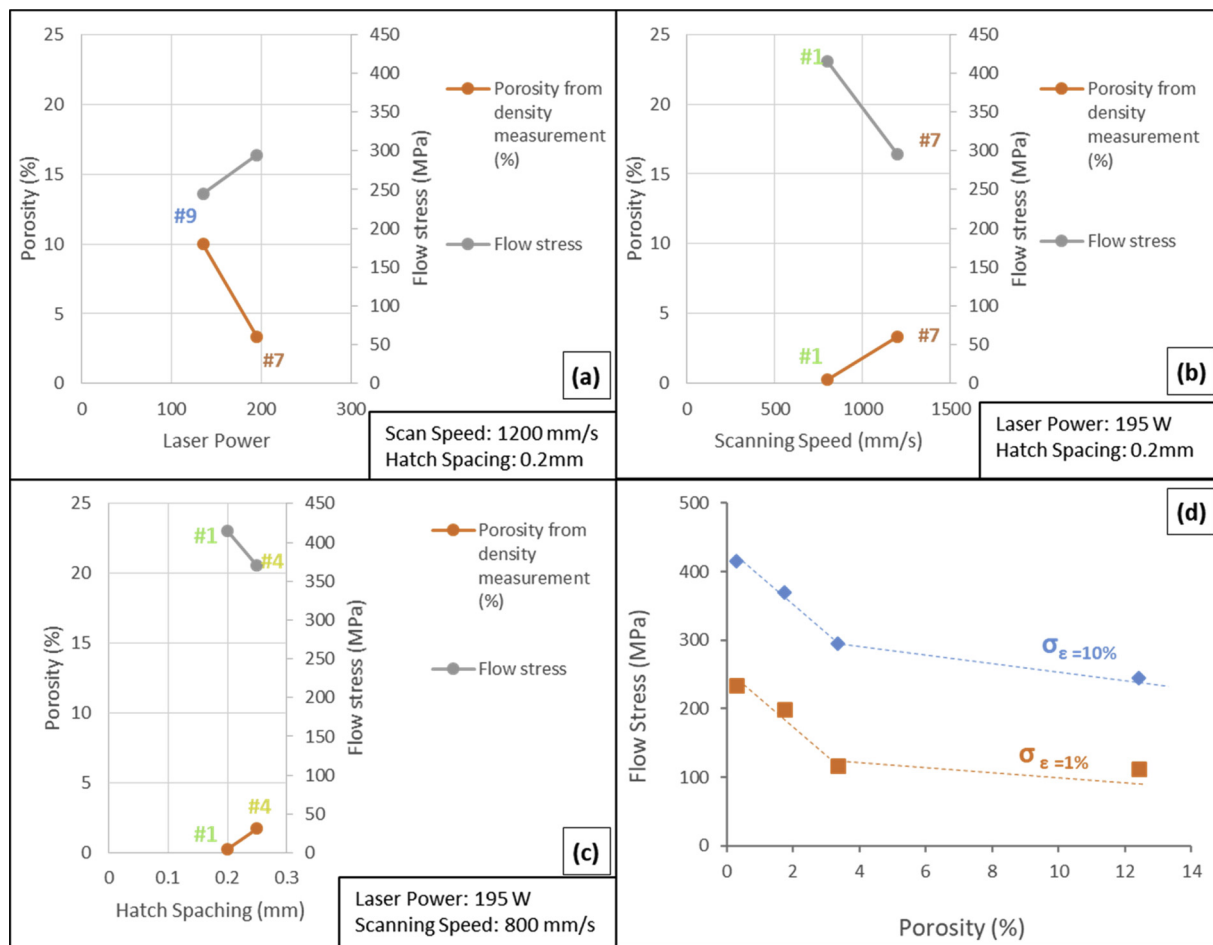


**Fig. 12.** The effect of variation in SLM processing parameters on porosity and dynamic strength of the WE-43 Mg additive builds. Variation in (a) laser power from 195 W to 135 W, (b) scanning speed from 800 mm/s to 1200 mm/s, and (c) hatch spacing from 0.2 mm to 0.25 mm. Higher laser power, slower scanning speed, and smaller hatch spacing are observed to reduce porosity along with an associated improvement in dynamic strength.

### 3.3.4. XRD

Selected area diffraction patterns (SADPs) from TEM showed only the matrix phase in HCP crystal structure, as observed in Fig. 8(d,f). It appears that none of the precipitates were coherent with the matrix, which rendered it extremely difficult to obtain any of their zone axes, so it was not possible to identify the crystal structure of the precipitates from SADPs. X-Ray diffraction was the only alternative and diffraction patterns of the as-built and HIP condition were analyzed, Fig. 11. While some precipitates of nano size like Mg-Nd ribbons in as-built condition (Fig. 6) might be too small, larger oxides and precipitates, like Mg-Y in Fig. 6, of palpable volume fractions are expected to be detected. Fig. 11 compares the diffraction patterns of as-built and HIP conditions of Sample#1. The main matrix Mg shows peaks of hexagonal structure P63/mmc with unit cell size  $a = 3.20956\text{\AA}$  and  $c = 5.21071\text{\AA}$ . The next phase with second largest peaks was  $\text{Y}_2\text{O}_3$  of cubic structure Ia3 (206) and unit cell length  $a = 10.604\text{\AA}$ . The high oxygen affinity of Y is expected to result in oxide formation in the raw material itself. These oxides were present in both as-built and HIP conditions and was detected by elemental segregation of Y and O in SEM-EDS (Figs. 6 and 9). While Zr also showed segregation into the same regions in the EDS, XRD did not reveal any YSZ or other Zr-, Y- rich oxides. The as-built condition also showed distinct peaks corresponding to  $\text{Mg}_{24}\text{Y}_5$  phase of cubic I43 m (217) structure with unit cell length  $a = 11.25\text{\AA}$ . SEM-EDS of as-built condition in Fig. 6 shows large Mg-Y precipitates, so these would be detected in XRD. Peaks corresponding to  $\text{Mg}_{24}\text{Y}_5$  were not detected in the HIP condition, conspicuous by the absence of peaks such as those at  $2\theta$  of  $40.9^\circ$ ,  $62.04^\circ$ , and  $67.4^\circ$ . The SEM-EDS of the HIP

condition in Fig. 9 verifies absence of large Mg-Y precipitates. The HIP condition showed an additional peak  $2\theta = 26.22^\circ$  which corresponds to  $\text{Mg}_{41}\text{Nd}_5$ , not observed in the as-built condition. SEM-EDS in Fig. 9 demonstrates the coarsening of Nd-rich precipitates during HIP treatment which appeared in XRD. But prior to HIP these Nd-rich ribbons were only 20–30 nm wide and would not have been detectable by XRD. Thus the XRD enabled confirmation of guesses from elemental segregation in EDS maps earlier, such as Y-rich oxides in both conditions (cubic  $\text{Y}_2\text{O}_3$ ), large Mg-Y precipitates (cubic  $\text{Mg}_{24}\text{Y}_5$ ) in as-built condition, formation of thicker Mg-Nd precipitates after HIP ( $\text{Mg}_{41}\text{Nd}_5$ ).

## 4. Discussion

The four as-built specimens together represent the effect of varying three of the SLM processing parameters. Samples #7 and #9 illustrate the effect of reducing laser power from 195 W to 135 W with constant scan speed of 1200 mm/s and hatch spacing of 0.2 mm. Fig. 12(a) compares the porosity and the flow stress of these two samples, showing that reduction in laser power resulted in a sharp rise in porosity to 12.4% along with a drop in strength from 295 MPa to 245 MPa. Similarly, Samples#1 and #7 depict the effect of increasing scanning speed from 800 mm/s to 1200 mm/s at a fixed laser power of 195 W and hatch spacing of 0.2 mm. The increase in scanning speed can be seen to result in an increase in porosity from 0.3% to 3.4% along with an associated drop in dynamic strength from 415 MPa to 295 MPa at 10% strain, Fig. 12(b). Fig. 12(c) compares the porosity reduction in Sample #1 to 0.3% compared to Sample # 4's 1.7% through reduction

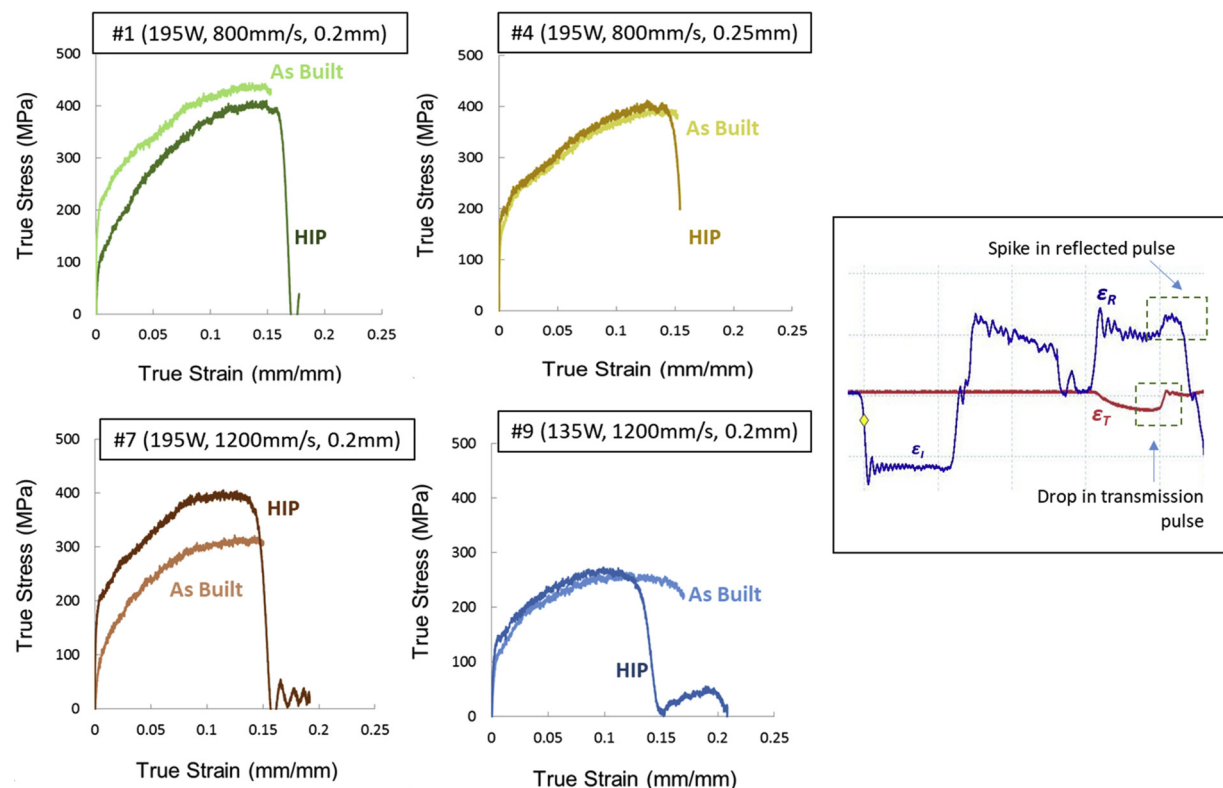


**Fig. 13.** Comparison of the dynamic stress-strain curves from SHPB testing at  $1000\text{ s}^{-1}$  on as-built vs. HIP'ed WE-43 Mg cylinders from the four SLM processing settings. Enclosed image on right: strain-gauge signals from SHPB test of HIP'ed Sample#1 showing incident ( $\epsilon_I$ ), reflected ( $\epsilon_R$ ) and transmission ( $\epsilon_T$ ) pulses with signature of failure. The spike in reflected pulse ( $\epsilon_R$ ) with a simultaneous drop in transmission pulse ( $\epsilon_T$ ) highlights the failure of the specimen.

of hatch spacing from 0.25 mm to 0.2 mm, while maintaining a constant high laser power of 195 W and slow scanning speed 800 mm/s. Higher laser power, slower scanning speed, and smaller hatch spacing are observed to reduce porosity along with an associated improvement in dynamic strength.

However, from Fig. 12(a–c) it is also clear that porosity is not always linearly related to strength. A large increase in porosity from 3.4% to 12.4% in Fig. 12(a) is associated with only a moderate strength loss. Whereas the porosity change from 3.4% to 0.3% in Fig. 12(b) is seen to associate with a significant spike in strength gain in Sample# 1 compared to Sample # 7. Fig. 12(d) plots flow stresses at 1% and 10% true strain of the as-built material as a function of its initial porosity. Sample#7 with 3.4% porosity had significantly lower strength (120 MPa at 0.01 strain) than Sample#1 with 0.4% porosity (240 MPa at 0.01 strain), a reduction of almost 50%. The drop in flow stresses at both 1% and 10% true strains was proportional (with similar slope across both) to the increase in porosity up to 3.4%. But Sample#9 with 12.4% porosity, had only a further strength drop of only 13% (250 MPa at 0.1 strain) from that of Sample#7 with 2.5% porosity (290 MPa at 0.1 strain). We have previously observed a similar trend in SLM Ti-6Al-4 V builds with induced porosity, but they showed steady drop in strength upto 45% porosity [43]. Here in the WE-43Mg builds, the strength drop is steeper at small levels of porosity but becomes moderate at porosities larger than 3.4%, similar to observations in 316 LSS and Al-Si-Cu and Al-Si-Mg alloys [44,45].

The nearly fully dense Sample#1 with 0.3% porosity showed an initial dynamic strength of  $\sim 240$  MPa increasing to  $\sim 420$  MPa by 0.1 strain. This is almost twice the dynamic strength of the cast WE-43, reported to remain below 200 MPa even at 0.1 strain by Xiang et al [31]. This is also higher strength than WE43-T5 alloy, precipitation hardened condition with large Zr-rich and cuboidal Y-rich precipitates, whose dynamic strength is below 320 MPa at 0.1 strain [31]. This superior strength of the additive builds can be attributed to two factors:

rapid solidification of SLM resulting in finer microstructures, and their complex microstructures with precipitates of various length scales in a hierarchical fashion, i.e. long ribbons of Nd-rich precipitates forming a eutectic like network, the minuscule Y-rich precipitates, and large Zr-Y-oxides.

The dynamic strength of the four sets of builds after HIP treatment is depicted in Fig. 13(b). It is clear that HIP treatment brought the responses of samples #1, #4, and #7 closer, even as the flow stresses of sample #9 remained much lower. In order to decipher the effect of HIP treatment, dynamic flow stresses of the as-built and HIP'ed conditions of each of the four builds are compared in Fig. 13. The nearly dense Sample#1 had an initial porosity of 0.3% in as-built condition, which did not improve palpably after HIP treatment remaining still around 0.3%. But Fig. 13 shows the strength of the HIP'ed build lower than as-built condition. Hence the drop must be owing to microstructural changes during HIP such as breaking up of Nd-rich ribbon precipitates. In Sample #4, the initial porosity of 1.7% is reduced to 0.6% after HIP treatment, and from Fig. 12(d) it is clear that at small porosities even such a small reduction of porosity can significantly improve strength. Therefore in Sample#4, the reduction in strength due to microstructural evolution during HIP treatment is overcome with improvement in strength with densification, and the flow stresses of the as-built and HIP'ed conditions are comparable. In Sample#7, the initial porosity of 3.4% is improved to 0.7% after HIP, a much higher advancement in densification and therefore greater strength enhancement. The HIP'ed condition of Sample#7 is stronger than the as-built condition. It can be observed that Sample#4 and Sample#7 with similar porosities after HIP treatment demonstrate comparable dynamic flow stresses. Sample#9 on the other hand had large initial porosity of 12.4%, which was recovered to 2.7% after HIP. From Fig. 12(d), it can be predicted that strength improvement would be small in this range of large porosities. Both as-built and HIP conditions of Sample#9 show alike and low dynamic flow stresses.

Another important observation was that all the HIP samples failed around 15% strain by 45° shear. This is recognizable in the raw strain gauge pulses from SHPB testing by the characteristic drop in the transmission pulse along with an associated spike in the reflected pulse (Fig. 13(right)) which is the signature of specimen fracture. After failure, the specimen cannot bear load and transfer the elastic wave, hence the broken sample reflects all of the incident wave back. Therefore the transmission pulse drops while the reflected pulse sees an upsurge simultaneously. The dynamic compression testing in SHPB at a high strain rate of 1000 s<sup>-1</sup> falls under adiabatic regime where the heat from plastic work is largely retained in the specimen, increasing the temperature of the specimen with accumulation of strain. The temperature rise at a given strain can be estimated from:

$$\Delta T(\varepsilon) = \frac{\eta \int_0^\varepsilon \sigma d\varepsilon}{\rho c_p}$$

where  $\sigma$  is the flow stress,  $\varepsilon$  is the strain,  $\rho$  is the density,  $c_p$  is the heat capacity and  $\eta$  is the conversion efficiency from mechanical energy to thermal energy. For metals, the value assigned to  $\eta$  is usually  $\sim 0.9$ . The area under the as-built Sample#1's curve is estimated to be  $\int_0^\varepsilon \sigma d\varepsilon \int_0^\varepsilon \sigma d\varepsilon \sim 42 \text{ N/m}^2$ . The density of this material is already calculated in Table 1 as 1.84 gm/cc while the heat capacity is reported by the manufacturer as 1 J/gm-C [39]. So the adiabatic temperature rise in Sample#1 after dynamic deformation to 0.15 strain is only 20 °C. Hamilton et al. reported that upon high velocity impact, commercial WE-43 Mg has been shown to form adiabatic shear bands with dynamic recrystallization [46]. But the strain rates of that study were approaching  $\sim 10^6 \text{ s}^{-1}$  simulating ballistic impact where the strain levels are also very high. Yokoyama et al reported 45° failure in wrought Mg alloys AZ31B-F, AZ61A-F, ZK60A-T5 under tensile SHPB testing at 1000 s<sup>-1</sup> at moderate strains  $\sim 20\%$  [47]. However, in the SLM WE-43 Mg specimens of this study, the as-built specimens clearly did not fail at the final strain of the test  $\sim 0.15$  strain while the post-HIP specimens all failed at that strain level. So this reduction in ductility has to be attributed to the microstructural evolution during HIP treatment rather than shear band formation tendency in the alloy.

## 5. Conclusions

Microstructure and dynamic mechanical behavior of WE-43 Mg alloy built through selective laser melting were investigated. Four different builds from varying parameter settings were examined in as-built and hot isostatically pressed conditions. The additive microstructures were exceedingly complex and hierarchical, composed of numerous features of various length scales. Both the as-built and HIP materials had large Y-, Zr-rich oxides. The as-built material had globular Y-rich precipitates as well as long-ribbon shaped Nd-rich precipitates. The HIP material had plate-like thicker Nd-rich precipitates and small globular Zr-rich precipitates. These additive builds showed much higher strength than the conventional cast and T5 treated alloys. The appearance of Zr-rich precipitates coincided with shear failures in HIP specimens at 0.15 true strain, while the breaking up of Nd-rich ribbon precipitates during HIP is associated with a drop in strength. HIP treatment was effective in densification at higher initial porosities but was unable to improve considerably at small porosity level due to the enclosed nature of the pores. Strength was highly dependent on the inherent porosity of these builds. Strength drop is steep even with introduction of low levels of porosity, but the drop steadily became leveled at higher porosities.

## Acknowledgment

The work was performed under cooperative agreement between Army Research Laboratory, University of North Texas, and Western Illinois University-Quad City Manufacturing Lab (W911NF-16-2-0189). We also acknowledge Materials Research Facility at the University of

North Texas for microscopy facilities.

## References

- [1] B.L. Mordike, Development of highly creep resistant magnesium alloys, *J. Mater. Process. Technol.* 117 (2001) 391–394.
- [2] Q.A. Lambri, W. Riehemann, Damping due to incoherent precipitates in commercial QE22 magnesium alloy, *Scr. Mater.* 52 (2005) 93–97.
- [3] H. Friedrich, S. Schumann, Research for a “new age of magnesium” in the automotive industry, *J. Mater. Process. Technol.* 117 (2001) 276–281.
- [4] N.A. El-Mahallawy, M.A. Taha, E. Pokora, F. Klein, On the influence of process variables on the thermal conditions and properties of high pressure die-cast magnesium alloys, *J. Mater. Process. Technol.* 73 (1998) 125–138.
- [5] T.M. Pollock, Weight loss with magnesium alloys, *Science* 328 (5981) (2010) 986–987.
- [6] N.V. Ravi Kumar, J.J. Blandin, M. Suéry, E. Grosjean, Effect of alloying elements on the ignition resistance of magnesium alloys, *Scr. Mater.* 49 (3) (2003) 225–230.
- [7] C. Liu, S. Lu, Y. Fu, H. Zhang, Flammability and the oxidation kinetics of the magnesium alloys AZ31, WE43, and ZE10, *Corros. Sci.* 100 (2015) 177–185.
- [8] L.L. Rokhlin, T.V. Dobatkina, I.F. Tarytina, V.N. Timofeev, E.E. Balakhehi, Peculiarities of the phase relations in Mg-rich alloys of the Mg-Y-Nd system, *J. Alloys. Compd.* 367 (2004) 17–19.
- [9] J.F. Nie, B.C. Muddle, Precipitation in magnesium alloy WE54 during isothermal ageing at 250°C, *Scr. Mater.* 40 (10) (1999) 1089–1094.
- [10] L. Gao, R.S. Chen, E.H. Han, Effects of rare-earth elements Gd and Y on the solid solution strengthening of Mg alloys, *J. Alloys. Compd.* 481 (1–2) (2009) 379–384.
- [11] J. Yan, Y. Sun, F. Xue, S. Xue, W. Tao, Microstructure and mechanical properties in cast magnesium–neodymium binary alloys, *Mater. Sci. Eng.* 476 (1–2) (2008) 366–371.
- [12] G.W. Lorimer, The Institute of Materials, LondonStructure-Property Relationship in Cast Magnesium Alloy Proceedings London Conference on Magnesium Technology, 1987, Structure-Property Relationship in Cast Magnesium Alloy Proceedings London Conference on Magnesium Technology (1987) 47–53.
- [13] J.F. Nie, X.L. Xiao, C.P. Luo, B.C. Muddle, Characterisation of precipitate phases in magnesium alloys using electron microdiffraction, *Micron* 32 (2001) 857–863.
- [14] J.J. Bhattacharyya, F. Wang, P.J. McQuade, S.R. Agnew, Deformation and fracture behavior of Mg alloy, WE43, after various aging heat treatments, *Mater. Sci. Eng.: A* 705 (2017) 79–88.
- [15] H. Li, F. Lv, X. Liang, Y. Qi, Z. Zhu, K. Zhang, Effect of heat treatment on microstructures and mechanical properties of a cast Mg-Y-Nd-Zr alloy, *Mater. Sci. Eng.: A* 667 (2016) 409–416.
- [16] R.A. Khosrshahai, R. Pilkington, G.W. Lorimer, P. Lyon, H. Karimzadeh, The microstructure and creep of as-cast and extruded WE54, *Proceedings of 3rd International Magnesium Conference* (1997) 241–256.
- [17] L.C. Zhang, H. Attar, Selective laser melting of titanium alloys and titanium matrix composites for biomedical applications: a review, *Adv. Eng. Mater.* 18 (2016) 463–475.
- [18] X. Wang, X. Gong, K. Chou, Review on powder-bed laser additive manufacturing of Inconel 718 parts, *Proceedings of the ASME 2015 International Manufacturing Science and Engineering Conference*, Charlotte, (2015) NC, USA, 8–12 June.
- [19] Z. Lu, J. Cao, H. Jing, T. Liu, F. Lu, D. Wang, D. Li, Review of main manufacturing processes of complex hollow turbine blades: this paper critically reviews conventional and advanced technologies used for manufacturing hollow turbine blades, *Virtual Phys. Prototyp.* 8 (2013) 87–95.
- [20] R.C. Oyagüe, A. Sánchez-Turrión, J.F. López-Lozano, J. Montero, A. Albaladejo, M.J. Suárez-García, Evaluation of fit of cement-retained implant-supported 3-unit structures fabricated with direct metal laser sintering and vacuum casting techniques, *Odontology* 100 (2012) 249–253.
- [21] T. Sercombe, X. Li, Selective laser melting of aluminium and aluminium metal matrix composites: review, *Mater. Technol.* 31 (2016) 77–85.
- [22] Matthias Gieseke, et al., “Selective Laser Melting of Magnesium and Magnesium Alloys.” *Magnesium Technology 2013*, Springer, Cham, 2013, pp. 65–68.
- [23] Chung Ng, Monica Savalani Chi, Hau Chung Man, Fabrication of magnesium using selective laser melting technique, *Rapid Prototyp. J.* 17 (6) (2011) 479–490.
- [24] Matthias Gieseke, et al., “Challenges of processing magnesium and magnesium alloys by selective laser melting.” European congress and exhibition on powder metallurgy. *European PM Conference Proceedings*. The European Powder Metallurgy Association, (2016).
- [25] D. Hu, Y. Wang, D. Zhang, L. Hao, J. Jiang, Z. Li, Y. Chen, Experimental investigation on selective laser melting of bulk net-shape pure magnesium, *Mater. Manuf. Process.* 30 (2015) 1298–1304.
- [26] B. Zhang, H. Liao, C. Coddet, Effects of processing parameters on properties of selective laser melting Mg-9%Al powder mixture, *Mater. Des.* 34 (2012) 753–758.
- [27] K. Wei, M. Gao, Z. Wang, X. Zeng, Effect of energy input on formability, microstructure and mechanical properties of selectively laser melted AZ91D magnesium alloy, *Mater. Sci. Eng. A* 611 (2014) 212–222.
- [28] M. Salehi, S. Maleksaeedi, H. Farnoush, M.L.S. Nai, G.K. Meenashisundaram, M. Gupta, An investigation into interaction between magnesium powder and Ar gas: Implications for selective laser melting of magnesium, *Powder Technol.* 333 (2018) 252–261.
- [29] T. Rzychon, A. Kielbus, Microstructure of WE43 casting magnesium alloy, *J. Achiev. Mater. Manuf. Eng.* 21 (1) (2007) 31–34.
- [30] P. Mengucci, Structure evolution of a WE43 Mg alloy submitted to different thermal treatments, *Mater. Sci. Eng.: A* 479 (2008) 37–44.
- [31] C. Xiang, Effect of microstructure on tensile and compressive behavior of WE43

- alloy as cast and heat treated conditions, *Mater. Sci. Eng.: A* 710 (2018) 74–85.
- [32] S. Agnew, Dynamic behavior of a rare-earth-containing Mg alloy, WE43B-T5, plate with comparison to conventional alloy AM30-F, *JOM* 66 (2) (2014) 277–289.
- [33] H. Asgari, On dynamic deformation behavior of WE43 magnesium alloy sheet under shock loading conditions, *Mater. Des.* 63 (2014) 552–564.
- [34] B. Nurel, M. Nahmany, N. Frage, A. Stern, O. Sadot, Split Hopkinson pressure bar tests for investigating dynamic properties of additively manufactured AlSi10Mg alloy by selective laser melting, *Addit. Manuf.* (2018).
- [35] Lucas Jauer, et al., "Selective laser melting of magnesium alloys." European congress and exhibition on powder metallurgy, European PM Conference Proceedings. The European Powder Metallurgy Association, (2016).
- [36] Rajiv Tandon, et al., Additive manufacturing of magnesium alloy powders: investigations into process development using elektron® MAP + 43 via laser powder bed fusion and directed energy deposition, European Congress and Exhibition on Powder Metallurgy. European PM Conference Proceedings. The European Powder Metallurgy Association, (2016).
- [37] WeinongW. Chen, Song Bo, Split Hopkinson (Kolsky) bar: design, testing and applications, Springer Science & Business Media (2010).
- [38] S. Gangireddy, S.P. Mates, High temperature dynamic response of a Ti-6Al-4V alloy: a modified constitutive model for gradual phase transformation, *J. Dyn. Behav. Mater.* 3 (4) (2017) 557–574.
- [39] Magnesium Elektron UK, Elektron 21, Datasheet 455, (2018) [https://www.magnesium-elektron.com/wp-content/uploads/2016/10/Elektron-21\\_1.pdf](https://www.magnesium-elektron.com/wp-content/uploads/2016/10/Elektron-21_1.pdf).
- [40] H.V. Atkinson, S. Davies, Fundamental aspects of hot isostatic pressing: an overview, *Metall. Mater. Trans. A* 31 (12) (2000) 2981–3000.
- [41] K. Essa, P. Jamshidi, J. Zou, M.M. Attallah, H. Hassanin, Porosity control in 316L stainless steel using cold and hot isostatic pressing, *Mater. Des.* 138 (2018) 21–29.
- [42] J. Groebner, light metal systems. Part 4: light metal ternary systems: phase diagrams, crystallographic and thermodynamic data, in: G. Effenberg, S. Ilyenko (Eds.), Chapter Mg-Nd-Y (Magnesium - Neodymium - Yttrium), 2006, pp. 343–350.
- [43] S. Gangireddy, E.J. Faierson, R.S. Mishra, Influences of Post-processing, Location, Orientation, and Induced Porosity on the Dynamic Compression Behavior of Ti-6Al-4V Alloy Built Through Additive Manufacturing, *J. Dyn. Behav. Mater.* (2018) 1–11.
- [44] Naci Kurgan, Effect of porosity and density on the mechanical and microstructural properties of sintered 316L stainless steel implant materials, *Mater. Des.* 55 (2014) 235–241.
- [45] Z. Ma, et al., A study of tensile properties in Al–Si–Cu and Al–Si–Mg alloys: Effect of  $\beta$ -iron intermetallics and porosity, *Mater. Sci. Eng. A* 490 (1–2) (2008) 36–51.
- [46] J. Hamilton, S.T. Brennan, Y. Sohn, B. Davis, R. DeLorme, K. Cho, Microstructural characteristics of High rate plastic deformation in elektron™ WE43 magnesium alloy, *Magnesium Technology 2012*, Springer, Cham, 2012, pp. 433–438.
- [47] T. Yokoyama, Impact tensile stress-strain characteristics of wrought magnesium alloys, *Strain* 39 (4) (2003) 167–175.